Surface Material Characterization from Non-resolved Multi-band Optical Observations

Doyle Hall[1], Kris Hamada[2], Thomas Kelecy[1], and Paul Kervin[3]

[1]*Boeing LTS, Kihei, Maui, HI and Colorado Springs, CO*
[2]*Pacific Data Solutions, Kihei, Maui, HI*
[3]*Air Force Research Laboratory, Kihei, Maui, HI*

1 SUMMARY

Ground-based optical and radar sites routinely acquire resolved images of satellites. These images provide the means to construct accurate wire-frame models of the observed body, as well as an understanding of its orientation as a function of time. Unfortunately, because such images are typically acquired at a single wavelength, this kind of analysis provides little or no information on the types of materials covering the satellite's various surfaces. Detailed surface material characterization generally requires multi-band radiometric and/or spectrometric measurements. Many widely-available instruments provide such multi-band information (e.g., spectrographs and multi-channel photometers). However, these sensors typically measure the brightness of sunlight reflected from the entire satellite, with no spatial resolution at all. Because such whole-body measurements represent a summation of contributions from many reflecting surfaces, an "un-mixing" analysis must be employed to characterize the reflectance of the satellite's individual sub-components. The objective of this paper is to outline the theory required for such an un-mixing process, focusing on two newly-developed analysis methods. Both methods retrieve satellite surface properties from temporal sequences of whole-body brightness measurements. Both require the following as input: 1) a set of multi-band measurements of a satellite's brightness in reflected sunlight, 2) the satellite's wire-frame shape model, including each major exterior sub-component capable of reflecting sunlight, 3) the satellite's attitude, specifying the orientation of all of the body's components at the times of each measurement. The first method also requires a library of bi-directional reflection distribution functions (BRDFs) for a set of candidate materials covering the satellite's surfaces, and yields estimates of the fraction of each satellite sub-component covered by each candidate material. The second method does not require pre-tabulated BRDFs, but instead attempts to retrieve BRDFs for each satellite sub-component from the non-resolved data using a series expansion approach.

This research funded by the Air Force Office of Scientific Research.

2 INTRODUCTION

Ground-based optical and radar sites routinely acquire resolved images of satellites, yielding a great deal of knowledge about orbiting spacecraft. In particular, the Air Force Maui Optical and Supercomputing (AMOS) Detachment on Maui has been acquiring optical imagery using two work-horse imagery systems. The AMOS Advanced Electro-optical System (AEOS) 3.6m telescope provides visible-band and long-wavelength thermal infrared images with adaptive optics compensation to remove atmospheric blurring. In addition, the AMOS Gemini 1.6m telescope system provides daytime visible-band and near-infrared speckle images. These systems reveal a great deal of resolvable detail for satellites in low-Earth orbit (LEO), especially after the data undergo post-processing enhancement at the AFRL Maui High Performance Computing Center. Other observatories, such as Starfire Optical Range (SOR), as well as some ground-based radar sites, also acquire images of comparable quality. From such images, detailed wire-frame models of the observed satellites can be assembled and aligned to the images. This process essentially translates the two-dimensional imagery into detailed three-dimensional information about the sizes, shapes, and relative orientations of various spacecraft components. Unfortunately, such image analysis procedures provide little or no information on the material and/or optical properties of the satellite surfaces, because the wire-frame models are typically based on single spectral band imaging data. Detailed surface material and property characterization generally requires multi-band photometric and/or spectrometric measurements.

3 ANALYSIS FORMULATION

The objective of this paper is to outline the theory required to retrieve satellite surface properties from temporal sequences of whole-body, multi-band brightness measurements, focusing on two newly-developed analysis methods. The first method, referred to here as "material abundance estimation" (MAE), seeks to determine the fractional abundances of materials covering the major exterior components of the observed satellite. This method has previously been described in detail and applied to simulated data of a convex object [1]. The second method, referred to here as "reflectance distribution estimation" (RDE), seeks to determine the bi-directional reflectance distribution functions (BRDFs) of the satellite's components.

Both analysis methods require three main types of input information: 1) a set of multi-band measurements of a satellite's reflected-sunlight brightness, 2) the satellite's wire-frame model, including each major exterior sub-component capable of reflecting sunlight, 3) the satellite's attitude, specifying the orientation of all of the body's components at the time of each multi-band measurement. The second two of these required inputs can be derived through a variety of means, including open-source publications or analysis of resolved imagery of the satellite (either pre-launch or on-orbit), as described previously [1]. The first input constitutes the data to be analyzed, and comprise observations from one (or more) sensors that provide non-resolved, multi-band brightnesses of the satellite. Such measurements naturally contain an abundance of information on the material-specific reflective properties of the satellite's surfaces. However, such spectrometric instruments often provide brightness measurements *of the entire object*, rather than from individual satellite surfaces or component. In other words, each measurement represents a summation of light reflected from many satellite components, thereby requiring an "un-mixing" analysis process to separate and retrieve individual component reflectance properties.

Because the first, MAE method seeks to estimate material abundances, it requires one additional input: pre-tabulated BRDFs for a set of candidate materials covering the satellite's surfaces. It then yields as output estimates of the fraction of each major satellite sub-component covered by each material. The MAE method can suffer significantly, however, when provided with a database not containing materials actually covering one or more components of the observed satellite [1], or not containing information on how the BRDFs change as materials experience space weathering effects. These two BRDF database limitations can potentially significantly limit the effectiveness of the MAE method when applied to unknown or aging satellites. The second, RDE method was developed specifically to address these limitations. It does not require any material BRDF information as input. Instead, the RDE method attempts to retrieve BRDF parameters for each satellite sub-component directly from the non-resolved data. For this reason, the RDE method promises to be more appropriate for analyses of objects covered with unknown or exotic materials or whose reflectance has changed significantly under the effects of space weathering.

3.1 Satellite Wireframe Shape Models

The required satellite wireframe models can be assembled by combining one or more data sources: design information provided by the manufacturer, pre-launch photographs and/or artistic renderings, and/or from resolved imagery of already-orbiting objects [1]. Wireframe models are typically assembled using primitive components (such as flat panels, spheres, cylinders, cones, parabolic dishes, etc.) combined to form accurate three-dimensional representations of all major exterior components of the satellite. After such model development is complete, each component of the wire-frame model can then be decomposed into a series of perfectly flat facets. Even round components may be approximated in this manner using many small facets. Each facet comprises a planar polygon with shape, area, and orientation derived from the original wire-frame model.

3.2 Satellite Attitude Models

Satellite attitude model can also be assembled in several ways. For instance, cooperative satellite owner/operators may willingly provide "quaternion data" encoding the detailed body attitude as a function of time, or at least provide the attitude control system (ACS) stabilization parameters employed on-board the satellite during the period of observations. Alternatively, analysis of high-quality images can provide the orientation of on-orbit satellites as a function of time, derived from the sequential frame-to-frame adjustments required to align the wire-frame model to a series of observed images [1]. Detailed image analysis can reveal ACS operational modes, or, alternatively, indicate rotational parameters for spin-stabilized satellites or even tumbling objects. Ultimately, this information can conceivably be used to assemble a predictive attitude model, and used as input by both of the analysis methods discussed here to specify the body's orientation at the time of each multi-band measurement.

In mathematical terms, the attitude model comprises the set of parameters required to specify the body's "attitude matrix," **R**, as a function of time. This 3×3 rotation matrix converts vectors from an inertial reference frame (taken here to be the Earth-centered J2000 frame) into the body-fixed reference frame, written symbolically as follows:

$$\mathbf{R} = \mathbf{R}(t) \tag{1}$$

where the time dependence indicates the changing orientation of the satellite. As an example, the attitude matrix provides the means to convert the inertial-frame satellite-to-observer and unit direction vector, $\mathbf{o}^*(t)$, and the satellite-to-Sun unit vector, $\mathbf{s}^*(t)$, into the body-frame through matrix multiplication:

$$\mathbf{o}(t) = \mathbf{R}(t)\ \ \mathbf{o}^*(t) \qquad\qquad \mathbf{s}(t) = \mathbf{R}(t)\ \ \mathbf{s}^*(t) \tag{2}$$

In this discussion, the "*" superscript denotes inertial-frame vectors, whereas body-frame vectors are denoted without superscripts. The two vectors given in Eq. (2) play an important role in determining the observed brightness of sunlight reflected from the body, as described below. While both of these vectors depend on time, in this discussion their explicit time dependence will often be suppressed for brevity.

3.3 Theory for Multi-band Un-mixing Analysis

The satellite wire-frame and attitude models described above provide a means of calculating the visibility and observation geometry of each resolved spacecraft surface during observations from any sensor with a known location. Notably, if one also had detailed *a priori* knowledge of the optical properties of each surface — i.e., the material composition, and associated material-specific bi-directional reflectance distribution functions (BRDFs) — then a forward model of the spectral signature of the entire body could be constructed by summing contributions from all reflecting surfaces visible to the sensor. However, in the absence of such *a priori* knowledge, characterizing the surface properties requires an un-mixing analysis of the whole-body multi-band measurements. Ideally, these measurements would be obtained by spectrometric instrumentation with good spectral resolution and a quick cadence. This would provide the spectral data required to discriminate different surface materials, and the temporal data to distinguish shiny and dull surfaces. The same task could also conceivably be performed by multi-channel photometer(s) providing relatively broad-band spectral coverage, albeit less efficiently.

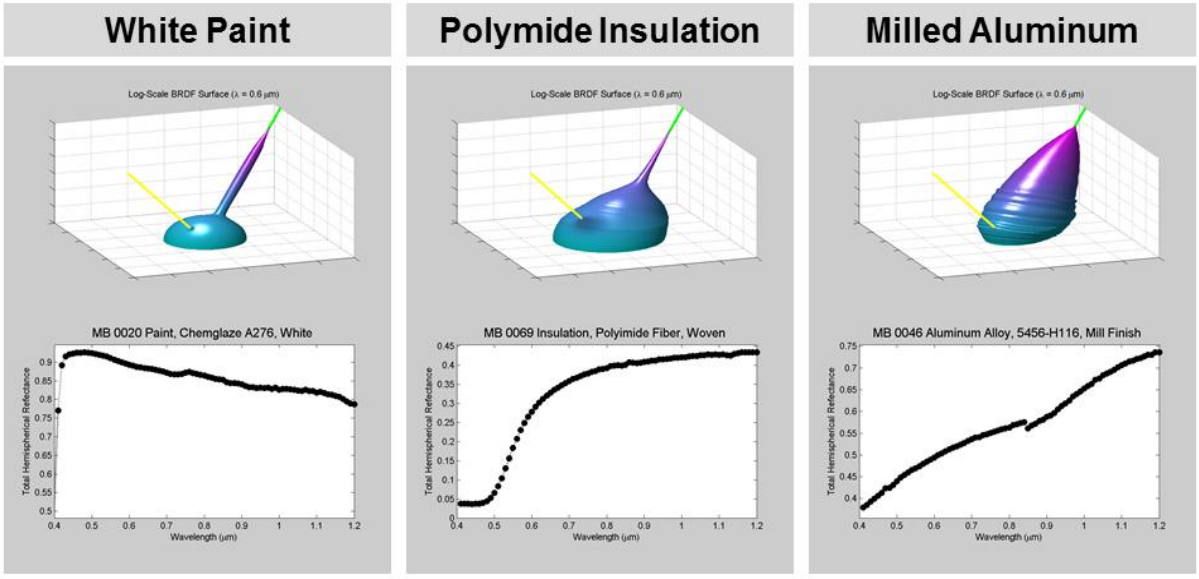

Figure 1. BRDF plots for three common spacecraft materials tabulated in the TASAT software package [2]. The top panels plot BRDF surface representations at a wavelength of $\lambda = 0.6$ μm, illustrating relative contributions of specular and diffuse reflection components. The yellow line indicates an example illumination direction, incident onto a reflecting sample of material lying in the bottom, horizontal plane. The green line shows the corresponding direction of specular reflection. Specular (or shiny) reflections appear as long and sharp spikes along this green line in these surface plots. The bottom panels plot the total hemispherical reflectance (i.e., albedo) spectra, spanning wavelengths $0.4 \le \lambda \le 1.2$ μm.

3.3.1 *The Spectral Intensity of a Satellite Reflecting Sunlight*

As discussed earlier, the wire-frame models provide the orientation and area of each facet of each satellite component. Specifically, the k^{th} facet of the j^{th} component may be characterized by its surface area, $A_{j,k}$, and normal unit vector, $\mathbf{n}_{j,k}$. These facets could, in principle, have time dependent orientations, $\mathbf{n}_{j,k}(t)$, such as those on articulating spacecraft structures, but this potential time dependence will be suppressed here for brevity. The spectral intensity (or spectral radiance), L, of sunlight reflected from the entire object has units of W ster^{-1} μm^{-1}. It is a function of both time and wavelength, and may be expressed as a summation over the component facets [1]:

$$L(t,\lambda) = F_{\text{Sun}}(t,\lambda)\left\{\sum_{j,k} A_{j,k}\,\langle \mathbf{n}_{j,k}\cdot\mathbf{o}\rangle\,\langle \mathbf{n}_{j,k}\cdot\mathbf{s}\rangle\;\rho_j(\lambda,\mathbf{n}_k,\mathbf{o},\mathbf{s})\;\Psi_{j,k}(\mathbf{o},\mathbf{s})\right\} \tag{3}$$

where $F_{\text{Sun}}(t,\lambda)$ denotes the illuminating solar irradiance (W m^{-2} μm^{-1}), $\mathbf{o}$ and $\mathbf{s}$ denote the time-dependent satellite-to-observer and satellite-to-Sun unit vectors from Eq. (2), and the function $\rho_j(\lambda, \mathbf{n}, \mathbf{o}, \mathbf{s})$ denotes the surface BRDF for satellite component j. Angular brackets denote the non-negative operator, $\langle x\rangle = \max(0,x)$, and the non-negative

dot products ensure that contributions arise only from facets showing an illuminated side to the observer. The shadowing/obscuration (SO) function, $\Psi_{j,k}(\mathbf{o}, \mathbf{s})$, denotes the fraction of each facet that is *not shadowed nor obscured* by other satellite surfaces. For convex bodies $\Psi_{j,k} = 1$ for all facets. For non-convex bodies this function generally varies with time. The relative positions and sizes of the satellite components specified in the wire-frame model, combined with the $\mathbf{o}(t)$ and $\mathbf{s}(t)$ unit vectors, provide a means to calculate the SO function using ray-tracing, z-buffering, or similar algorithms (the currently-implemented MAE and RDE methods employ z-buffering).

3.3.2 *Material Bi-directional Reflectance Distribution Functions (BRDFs)*

Notably, the satellite wire-frame and attitude models together provide all of the quantities required to calculate the spectral intensity using Eq. (3), *except* for the BRDFs. In fact, the importance of the wavelength-dependent BRDF in Eq. (3) cannot be overemphasized in this regard. It basically indicates how multi-band measurements can be used to diagnose the material composition, and is fundamental to the feasibility of the un-mixing analyses. Many groups have measured material BRDFs in laboratory environments and/or created numerical BRDF models. For instance, BRDFs for several spacecraft materials — such as solar array panels, milled aluminum, anodized aluminum, multi-layer insulation, white paint, etc. — are available as part of the TASAT satellite radiometry simulation software package [2]. Fig. 1 illustrates BRDFs for three common satellite materials tabulated in the TASAT database [1]. Material BRDFs contain two general types of information that can help identify and discriminate satellite materials. First BRDFs contain spectral "fingerprints" (Fig. 1, bottom panels). These are wavelength-dependent patterns in the reflectance (i.e. albedo) that can uniquely identify the material composition [3, 4]. BRDFs for different materials also vary significantly in their relative fractions of specular vs. diffuse (i.e., shiny vs. dull) reflectance. The two analysis methods presented here exploit both of these aspects of BRDFs. The MAE method focuses using a database of candidate material BRDFs to estimate the abundances of materials on exterior satellite components. The RDE method seeks to estimate the BRDF of each satellite component using a series expansion approach.

3.3.3 *Analysis Method 1: Material Abundance Estimation (MAE)*

As a first step, the MAE formulation assumes that the surfaces of each satellite component can be modeled as a mixed set of distinct materials compiled in a BRDF database [1]. In this case, the *effective* BRDF for the k^{th} facet of the j^{th} satellite component may be written as a sum over the individual material BRDFs as follows:

$$\rho_j(\lambda, \mathbf{n}_{j,k}, \mathbf{o}, \mathbf{s}) = \sum_m f_{j,m}\ \beta_m(\lambda, \mathbf{n}_{j,k}, \mathbf{o}, \mathbf{s}) \tag{4}$$

where $f_{j,m}$ denotes the fractional area of component j covered by material m, and $\beta_m(\lambda, \mathbf{n}, \mathbf{o}, \mathbf{s})$ denotes the pre-tabulated, laboratory-measured BRDF for the pure material m. Inserting Eq. (4) into Eq. (3) and re-arranging yields:

$$L(t,\lambda) = \sum_{j,m} f_{j,m}\ K_{j,m}(t,\lambda) \tag{5}$$

where the kernel function is

$$K_{j,m}(t,\lambda) = F_{\text{Sun}}(t,\lambda)\left\{\sum_k A_{j,k}\ \langle \mathbf{n}_{j,k}\cdot\mathbf{o}\rangle \langle \mathbf{n}_{j,k}\cdot\mathbf{s}\rangle\ \beta_m(\lambda, \mathbf{n}_{j,k}, \mathbf{o}, \mathbf{s})\ \Psi_{j,k}(\mathbf{o}, \mathbf{s})\right\} \tag{6}$$

Notably, this kernel can be readily calculated because all of its component quantities are known from either independent measurement (such as the solar flux and the database of laboratory-measured BRDFs) or from the wire-frame and attitude models. The only remaining unknown quantities in Eq. (5) are the fractional areas (i.e., "abundances") covered by the pure materials, $f_{j,m}$. These quantities are subject to the following two constraints:

$$0 \le f_{j,m} \le 1 \qquad \sum_m f_{j,m} = 1 \tag{7}$$

The objective of the MAE process is to find the set of fractional areas, $f_{j,m}$, that best reproduce the observed spectral radiance data but that also satisfy these two constraints.

Typical long-slit spectrographs or broad-band photometric instruments do not provide continuous measurements of the spectral intensity, $L(t, \lambda)$, but instead provide observations at a discrete set of times, $\{t_i,\ i=1\ldots N_i\}$ and wavelengths, $\{\lambda_l,\ l=1\ldots N_l\}$. This formulation idealizes each of these measurements as instantaneous (i.e.,

neglecting the finite exposure time spanned by each measurement) with perfectly narrow wavelength sampling (i.e., neglecting the finite width of each spectral channel). With these assumptions, the spectrometric measurements can be organized into a discrete matrix as follows:

$$L_{i,l} = L(t_i, \lambda_l) \tag{8}$$

and Eq. (5) can be used to write the system of equations that must be solved in the inversion process

$$L_{i,l} = \sum_{j,m} f_{j,m} \; K_{i,l,j,m} \tag{9}$$

At this point, it is convenient to combine indices to streamline the formulation. The two observation indices (i, l) can be combined into one master index, μ, spanning $\mu = 1 \ldots N_i N_l$. Similarly, the indices (j,m) can be combined into a master index ν. Using these master indices, Eq. (9) can be re-written in a relatively simple form:

$$L_{\mu} = \sum_{\nu} f_{\nu} \; K_{\mu,\nu} \tag{10}$$

At first glance, Eq. (10) appears to be a linear system, which could be solved using a variety of methods such as a least-squares analysis using singular-value decomposition or using the pseudo-inverse matrix formalism [5]. However, the constraints stated in Eq. (7) still must be satisfied, making such methods inappropriate. Fortunately, there are efficient numerical methods [6, 7] that do provide a means of imposing such constraints (pre-programmed into the Matlab software system as function *lsqlin*). Solving Eq. (10) using such methods provides the set of f_ν or, alternatively, $f_{j,m}$, which represent the best-fit fractional areas of each satellite component covered by each reflective material.

3.3.4 *Analysis Method 2: Reflectance Distribution Estimation (RDE)*

The RDE method does not assume that the satellite components can be modeled as a mixture of known materials, as does the MDE method. Instead, the RDE method attempts to estimate the BRDF of each satellite component using a series expansion approach. In this case, the model BRDF for the k^{th} facet of the j^{th} satellite component may be written as a sum over a set of BRDF expansion functions as follows:

$$\rho_j(\lambda, \mathbf{n}_{j,k}, \mathbf{o}, \mathbf{s}) = \sum_m a_{j,m} \; \beta'_m(\lambda, \mathbf{n}_{j,k}, \mathbf{o}, \mathbf{s}) \tag{11}$$

where $a_{j,m}$ denotes the albedo of component j associated with the BRDF expansion function β'_m (λ, **n**, **o**, **s**). These BRDF expansion functions do not correspond to pure materials, but instead are analytical functions that span a range of reflectance distributions from very dull (diffuse) to very shiny (specular), as illustrated in Fig. 2. In this formulation, these expansion functions have the following form:

$$\beta'_m(\mathbf{n}, \mathbf{o}, \mathbf{s}) = \begin{cases} 1/\pi & m = 0 \\ \beta_{\text{CT}}(\mathbf{n}, \mathbf{o}, \mathbf{s}, \mu_m) & m = 1 \ldots N_{\text{SPEC}} \end{cases} \tag{12}$$

The m = 0 component represents purely diffuse reflection using the simple Lambertian BRDF. The remaining components represent increasingly specular reflection using analytical functions based on the "Cook-Torrance" formulation [8]. This series expansion approach assumes that real-world BRDFs, such as the surfaces shown in Fig. 1, can be approximated sufficiently using a weighted sum of analytical functions, like those in Fig. 2.

One choice for series expansion functions is based on the Cook-Torrance BRDF formulation [8], used here because it is both physics-based and relatively computationally efficient. The underlying assumption for this formulation is that most surfaces are uneven at a size scale comparable to or larger than the wavelength of reflected light. BRDFs for such "rough" surfaces must account for the collective reflection, shadowing and obscuration from the "micro-facet distributions" of the surfaces [9, 10], and have *effective specular components* that form broad distributions peaked in the direction of perfect mirror-like reflection. The exact form of these broadened peaks depends on the parameters of the micro-facet distributions. However, the Cook-Torrance formulation [8] uses a single, physics-based parameter — μ, the RMS slope of the micro-facets — to specify the width of the specular peak as follows:

$$\beta_{\mathrm{CT}}(\mathbf{n},\mathbf{o},\mathbf{s},\mu)=\left[\frac{1}{\pi(\mathbf{n}\cdot\mathbf{o})(\mathbf{n}\cdot\mathbf{s})}\right]\left[\frac{e^{-(\tan\alpha/\mu)^2}}{4\mu^2\cos^4\alpha}\right]\left[\min\left(1,\frac{2(\mathbf{n}\cdot\mathbf{b})(\mathbf{n}\cdot\mathbf{o})}{(\mathbf{o}\cdot\mathbf{b})},\frac{2(\mathbf{n}\cdot\mathbf{b})(\mathbf{n}\cdot\mathbf{s})}{(\mathbf{o}\cdot\mathbf{b})}\right)\right] \tag{13}$$

where α the angle between the surface normal, **n**, and the vector **b**, which bisects the **o** and **s** vectors. The first two factors in Eq. (13) account for the collective reflection from the micro-facet distribution and the last for micro-facet shadowing/obscuration effects [8], not to be confused with the macroscopic facet SO function introduced in Eq. (3). The set $\{\mu_m\}$ in Eq. (12) should span the range of RMS slopes representative of common materials; something like $0.04 \le \mu_m \le 0.5$ [see 8].

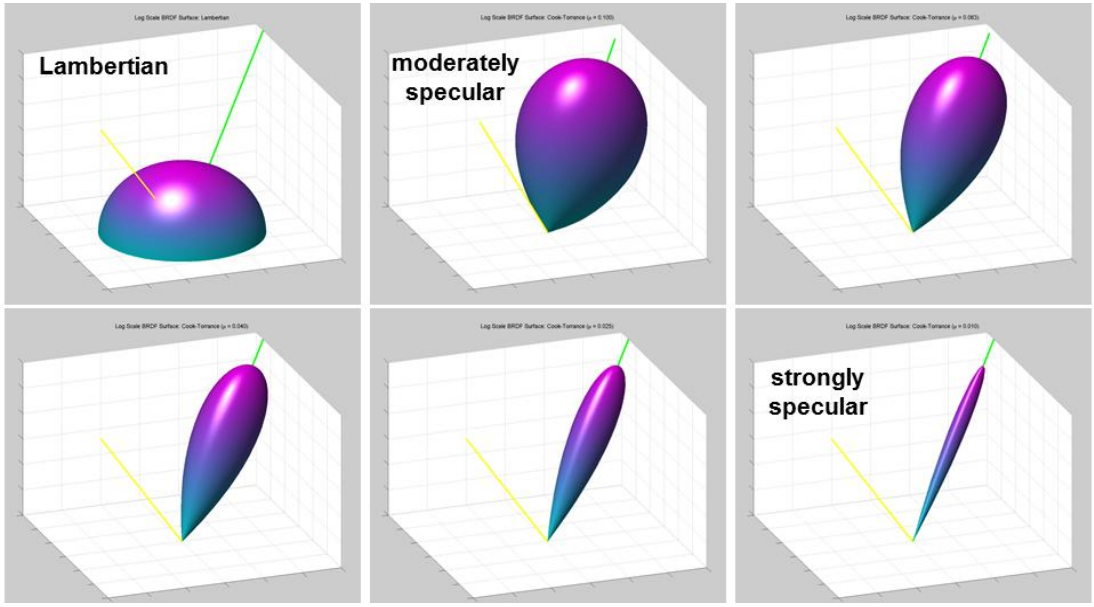

Figure 2. Surface plots for six BRDF expansion functions used in the RDE method, spanning diffuse reflection (upper left) to strongly specular reflection (lower right). In each plot, the yellow line indicates an incident illumination direction, and the green line the corresponding direction of specular (i.e., mirror-like) reflection. Strongly specular BRDFs are dominated with long, sharp spikes along this green line (lower right panel). Diffuse BRDFs don't have such directionality; in fact, perfect Lambertian reflectors have hemi-spherical surfaces (upper left).

Inserting Eq. (11) into Eq. (3) and re-arranging yields:

$$L(t,\lambda)=\sum_{j,m} a_{j,m}\; K'_{j,m}(t,\lambda) \tag{14}$$

where this kernel function has similar form to that given in Eq. (6), and also can be readily calculated because all of its component quantities are known from either independent measurement, the wire-frame and attitude models, or from the BRDF expansion functions. The only remaining unknown quantities in Eq. (14) is the set $\{a_{j,m}\}$, which denote the albedo of component *j* associated with the BRDF expansion function *m.* These are subject to the following two constraints:

$$0 \le a_{j,m} \le 1 \qquad\qquad a_j \equiv \sum_m a_{j,m} \;\le 1 \tag{15}$$

The objective of the RDE analysis is to find the set of albedos $\{a_{j,m}\}$ that best reproduce the spectral radiance data but that also satisfy these two constraints. Note that the second of these constraints differs from the MAE method, in that it is *summation equality constraint* rather than a *summation inequality constraint.* Fortunately, both can be handled by available numerical methods [6, 7]. Solving for the best-fit set $\{a_{j,m}\}$ can formulated and performed in a fashion very similar to the MAE method described above. Eqs. (11)-(13) can be then used to calculate the best estimate of the BRDF for each satellite component, $\rho_j(\lambda,\ \mathbf{n},\ \mathbf{o},\ \mathbf{s})$.

4 APPLICATION TO SIMULATED OBSERVATIONS

This section applies the two analysis method to simulated observations of a relatively simple non-convex model satellite, as shown Fig. 3 and detailed in Table 1. Simulated spectral irradiances were calculated using TASAT

BRDFs and Eq. (3). Fig. 4 shows simulated brightnesses for this satellite during the fully-sunlit portions of two LEO terminator passes over the Maui AMOS site and the South American SOAR sites. The analyses presented below employ simulations from these two ground-based sites, including the passes shown in Fig. 4 and other qualitatively-similar additional ones.

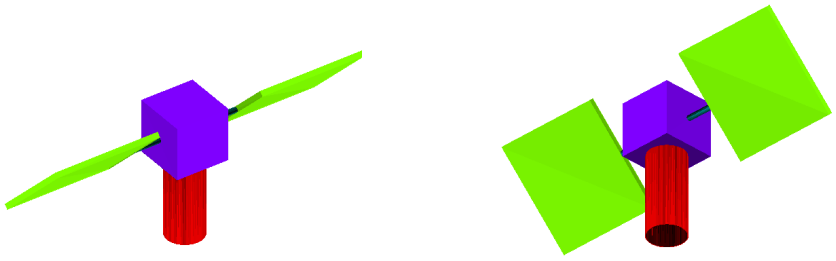

Figure 3. Schematic illustrations showing two views of the simple, non-convex satellite used for spectral radiance simulations and testing of the MAE and RDE analysis methods, comprising four distinct components color-coded as follows: "buscube" (purple), "bustube" (red), "wings" (green), and "struts" (blue). See Table 1 for details on the specific material and BRDFs covering each of these components. For size scale, the sides of the purple cube measure 1 m, and the red tube 1.5 m in length.

Component Index, *j*	Short Name	Component color in Fig. 3	BRDF Type	TASAT BRDF	Material Description, finish and other details
1	Bustube	Red	Maxwell Beard	0046	Aluminum Alloy, 2024-T3
2	Wings	Green	Maxwell Beard	0020	Solar Cell, Silicon, Sun Side
3	Struts	Blue	Maxwell Beard	0029	Aluminum Alloy, 5456-H116, Mill Finish
4	Buscube	Purple	Maxwell Beard	0069	Insulation, Polyimide Fiber, Woven

4.1 Results for Method 1: Material Abundance Estimation (MAE)

The MAE analysis method has previously been applied to a convex object [1], along with tests of truth retrieval from noise-free scans, as well as discussions of the limitations of noisy measurement data and BRDF databases that are either incomplete and/or possess superfluous materials that are not found anywhere on the observed satellite. These general results and conclusions apply equally well to the non-convex satellite analyzed here, and will not be restated in the interest of brevity. Instead, this analysis focuses on results from simulations of noisy, multi-site, ground-based observations of the satellite in LEO, using the same plot formats and notation introduced in [1].

4.2 Results for Method 2: Reflectance Distribution Estimation (RDE)

The RDE method has a much grander objective than the previously-described MAE method, in that it seeks to derive the complete reflectance distribution functions for the entire set of satellite components, rather than just a simple mixture of materials for each. Perhaps the most important lesson learned from the development and testing of these two analysis methods is that the RDE method, when compared to the MAE method, requires a much larger amount of data with significantly greater geometric diversity to converge to accurate results. Evidently, to derive accurate specular reflection components, the observations must sample each satellite component glinting, ideally from several perspectives. In other words, the data must sufficiently sample the "sharp peaks" of the BRDF surfaces, such as those shown in Fig 1. Achieving this requires a tremendous quantity of diversity in observational geometry (i.e., richly varied viewing and illumination perspectives).

In fact, it turns out that the RDE method can suffer numerical instability when provided with input data of limited geometrical diversity. The reason for this is that it often has no data to constrain the albedos of the sharpest specular components in the retrieved BRDF expansion series. In other words, the amplitude of the specular BRDFs shown on the lower-right of Fig. 2 can grow unphysically large, simply because few (or no) observations provided data that sampled that specular peak. This manifests itself in the component albedos, a_j, approaching unity, because the most-specular component albedos, $a_{j,m}$, have grown to large values. However, there is a numerical means of addressing this instability. Specifically, imposing the inequality constraints of Eq. (15) employs Lagrange multipliers [6, 7], one for each BRDF expansion function m. These multipliers can be inspected to determine if this kind of instability in the most specular BRDF(s) has manifested itself in the solution. If that is found to be the case, then these affected BRDFs can be eliminated from the expansion function set, the corresponding $a_{j,m}$ values set to zero, and the process repeated until a numerically stabilized solution is found. The resulting solution set $\{a_{j,m}\}$ can then be inserted into Eqs. (11)-(13) to calculate the best-fit BRDF for each satellite component, $\rho_j(\lambda, \mathbf{n}, \mathbf{o}, \mathbf{s})$.

Table 1. Materials and BRDFs used for satellite components in the spectral radiance simulations.

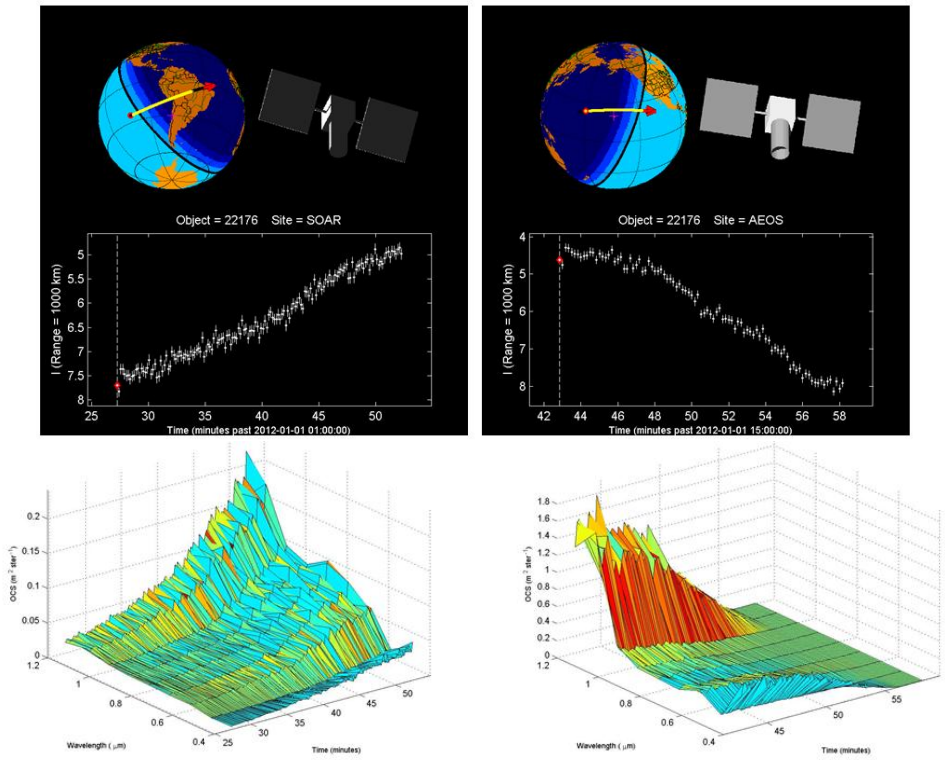

Figure 4. Simulated ground-based observation of the non-convex satellite shown in Fig. 3 flying in the orbit of SSN 22176 making passes over SOAR in Chile (left) and AMOS on Maui (right) on 2012 Jan 01. The simulation assumes nadir/velocity stabilization, with the red tube of the satellite pointed along the nadir direction and the solar panel struts aligned along the velocity direction. The dark panels at the top shows temporal signatures along with renderings of the cube reflecting sunlight (upper right), its position along the ground-track (upper left) and the whole-body I-band (λ = 0.8 μm) brightness in range-normalized stellar magnitudes (plotted for fully sunlit conditions). The bottom panels show surface plots of the associated multi-band OCS values for each pass, used as input to the MAE and RDE analyses [1]. The simulations used in this analysis employ 9 bands (0.2, 0.4, 0.6, 0.8, 1.0, and 1.2 μm) and assume 10% Gaussian noise on the OCS measurements.

Fig. 5 shows the results of the MAE method applied to progressively increasing amounts of ground-based data. The three panels show the results from one, three, and six terminator passes from left to right. It demonstrates that adding more data to the process leads to progressively improved MAE results. It also demonstrates that the smallest-sized component of the satellite (the struts in Fig. 3 and Table 1), which naturally reflects less light than the other larger components, requires the most data in order to converge to accurate material abundance results.

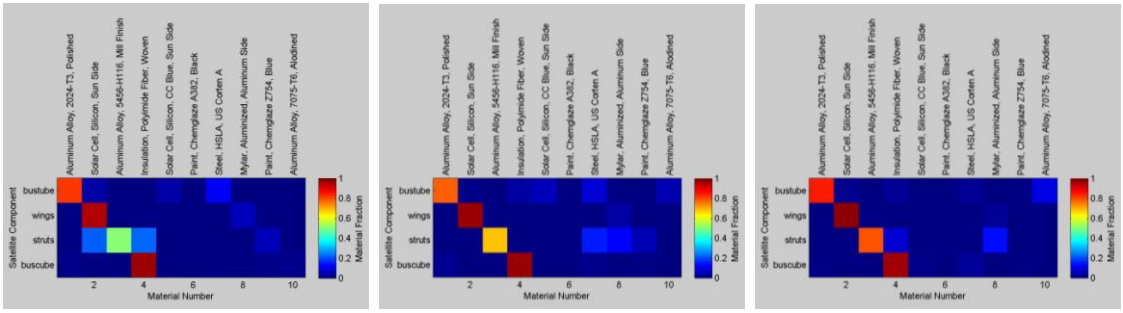

Figure 5. Estimated material abundances, $f_{j,m}$, derived by combining using increasing numbers of passes of data. The three panels show the results from one SOAR ground-based pass (left), three passes spanning one day (1 SOAR + 2 AMOS, center), and six passes spanning two days (2 SOAR + 4 AMOS, right). Each plot shows the four satellite components (described in Table 1) along the vertical axis and twelve candidate materials along the horizontal axis. A diagonal pattern red-squares ($f_{j,m}$ = 1 along the diagonal and $f_{j,m}$ = 0 elsewhere) in the first four columns of each plot represents perfect truth retrieval [see 1]. As can be seen in this progression, adding more data to the process leads to progressively improved MAE results that approach perfect truth on the right panel.

Fig. 6 shows the best-fit BRDFs (along with known truth), derived using an RDE analysis of 8 days worth of data from the two sites (a total of 18 passes) on the nadir-velocity stabilized model satellite. A close inspection of the BRDF surfaces and albedo spectra plotted in Fig. 6 clearly shows that, even with this large number of passes, the method really has not converged to known-truth reasonable accuracy (recall that the MAE method converged to reasonable accuracy using just 6 passes). Evidently, even eighteen passes observed from these two ground-based sites still does not provide sufficient geometric diversity. Two ways to achieve more geometric diversity for such a

stabilized satellite would be to add more ground-based sites, and/or ever larger numbers of observed passes. However, this research indicates that a far more efficient way is to employ one (or more) space-based sensors, which provide more dramatic changes in viewing and illumination perspectives on much shorter time-scales than can be reasonably achieved even with a very large number of ground-based sensors. Preliminary analysis indicates that after including two or three ground-based sites with good global coverage (especially in latitude), adding a single space-based sensor provides by far the best means of enriching observational diversity when observing satellites already in orbit.

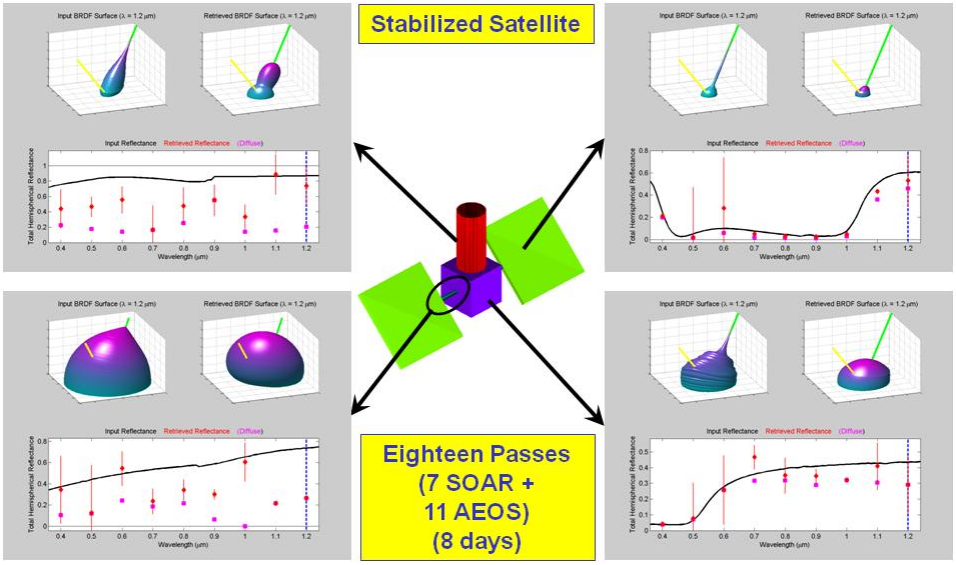

Figure 6. Estimated BRDFs derived by combining using 18 passes of data on the nadir-velocity stabilized satellite. The four outer-most panels show the known-truth and reconstructed BRDF surfaces (top left and right, respectively) and the known-truth and reconstructed albedo spectra (bottom), plotted in black curves and as the red points, respectively. The red points represent the best-estimate total albedos for each of the 9 bands in the simulated data set, and error bars account for the "best-fit uncertainty" of each point, but not for any deficiencies in the BRDF series-expansion model. The pink points in each plot show the estimated Lambertian fraction of the albedo. Each panel shows the results for the four satellite components described in Table 1, as shown by the arrows emanating from the central rendering of the model satellite. As can be seen, even a total of eighteen complete terminator passes, compiled over eight days of observations from the two ground-based sites, do not provide sufficient geometric diversity to converge accurately to the known-truth BRDFs for this nadir-velocity stabilized satellite.

Changing an object's attitude can also provide increased geometric diversity. Three-axis satellite stabilization, such as the nadir-velocity attitude used in the previously-analyzed simulations, tends to significantly limit geometric diversity because it produces very slow changes in the relative orientation of the sensor(s) and the Sun. Generally, an observer would not be able to change an orbiting object's attitude without, at the very least, cooperation from the satellite's owner/operator. However, an object's attitude can easily be changed in a laboratory observation environment, or in simulation studies. Laboratory-based tests of the RDE method would therefore benefit greatly by using multi-perspective observations, achieved perhaps by mounting the object on an articulating robot arm, or on a rotating platform. Along these lines, our simulation studies indicate that rotational motion naturally provides a great deal of geometric diversity, and significantly enhances the accuracy of RDE method analyses. Furthermore, more complicated rotational motion produces greater diversity. So an object in a complex, three-axis rotation state (e.g., precession+nutation) would generally produce more diversity than an object in a stable spin (i.e., a single-axis state).

Fig. 7 shows the estimated BRDFs (along with known truth) derived using an RDE analysis of the same 8 days worth of simulated data from the two ground-based sites as shown in Fig. 6, but with the satellite in a three-axis rotation state, with the rotation rates about each axis in the range of 1 to 3 degrees per second, so that the object undergoes several complete rotations in all axes during each observed pass. As can be seen in Fig. 7, this dramatic increase in geometric diversity allows the RDE method to converge close to known-truth with reasonable (but not perfect) accuracy. The remaining differences between the known-truth and best-fit BRDF surfaces (top plots in the four outer-most panels of Fig. 7), as well as in the known-truth and best-fit albedos (the black curves and red points in the bottom plots of the four panels) are likely due to a combination two inadequacies of the current RDE implementation: 1) that too few terms were used in the BRDF series expansion, and/or 2) that the Lambertian + Cook-Torrance analytical functions themselves cannot capture all of the relevant aspects of real-world BRDFs. Resolving these remaining discrepancies, and determining more specifically what constitutes sufficient geometric diversity for the CDE method to converge accurately, requires further simulation and/or laboratory studies.

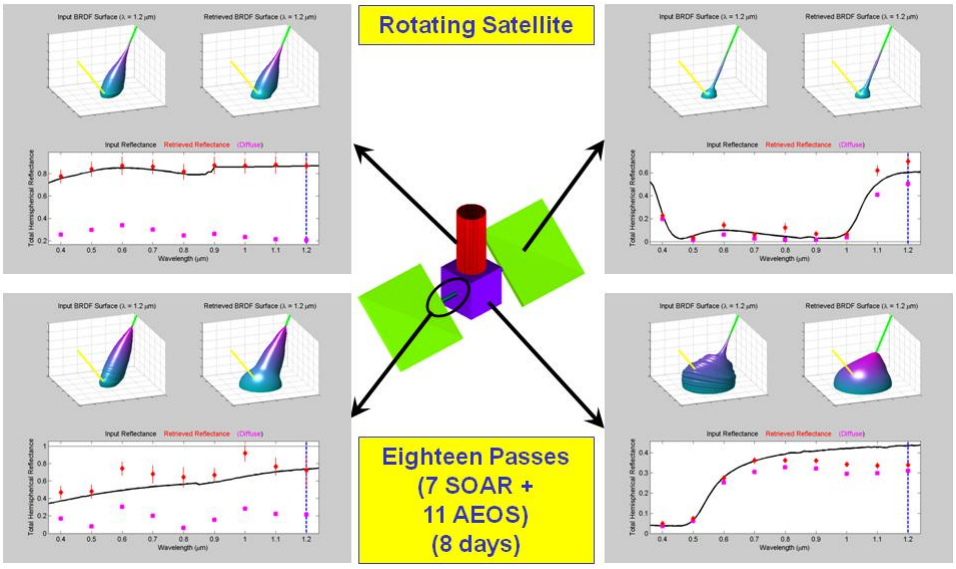

Figure 7. Estimated BRDFs derived from data on a rotating satellite, shown in a format similar to that of Fig. 6. The added geometric diversity naturally provided by the object's rotational motion allows the RDE analysis to converge much more accurately to the known-truth BRDFs. The remaining differences between the known-truth and best-fit BRDF surfaces (top plots in the four outer-most panels), as well as in the known-truth and best-fit albedos (the black curves and red points in the bottom plots of the four panels) are due to a combination of inadequacies in the number of terms used in the BRDF series expansion, and/or the in the quality of the BRDF basis functions themselves.

5 CONCLUSIONS AND FUTURE WORK

This paper presents the theory required to retrieve satellite surface properties from temporal sequences of whole-body, multi-band brightness measurements, focusing on two new analysis methods. The first, *material abundance estimation* (MAE), determines the abundances of materials covering the components of the observed satellite. The second, *reflectance distribution estimation* (RDE), determines the BRDFs of the satellite's components. The MAE method can suffer from the limitations of the BRDF database of candidate materials that it requires, making it inappropriate for unknown or aging satellites. The RDE method was developed specifically not to need such a database, but instead estimate BRDFs for each of the satellite's components using a series expansion approach. The RDE method requires data with significant geometric observational diversity, in order to converge with reasonably accuracy. Employing multiple ground-based sites can help provide such diversity, but a much more efficient approach would be to use even a single space-based sensor. Further analysis needs to be conducted to determine if achieving sufficient diversity for stabilized satellites is even possible, and if so, if it requires a prohibitive number of ground- and/or space-based observations.

6 REFERENCES

1. Hall, D., "Surface Material Characterization from Multi-band Optical Observations", *2010 AMOS Technical Conference*, Wailea, Maui, Hawaii, 15-17 September 2010.
2. Riker, J., and Butts, R., "The Time-Domain Analysis Simulation for Advanced Tracking (TASAT) Approaches to Compensated Imaging", SPIE Vol.1688, *Atmospheric Propagation and Remote Sensing*, 1992.
3. Jorgensen, K.,"Using Reflectance Spectroscopy to Determine Material Type of Orbital Debris", Ph.D. Thesis, Univ. of Colorado, Boulder, May 2000.
4. Jorgensen, K., Okada, J., Guyote, M., Africano, J., Hall, D., Hamada, K., Barker, E., Stansbery, G., and Kervin, P., "Reflectance Spectra of Human-made Objects", *2004 AMOS Technical Conference*, Wailea, Maui, Hawaii, 13 –17 September 2004.
5. Press, W. et. al., "Numerical Recipes in FORTRAN: The Art of Scientific Computing" (2nd Edition), Cambridge University Press, New York NY, 1992.
6. Coleman, T.F., and Li, Y., "A Reflective Newton Method for Minimizing a Quadratic Function Subject to Bounds on Some Variables", *SIAM J. on Optimization*, Vol.6, No.4, 1040-1058, 1996.
7. Gill, P.E, Murray, W., and Wright, M.H., "Practical Optimization", Academic Press, London, UK, 1981.
8. Cook, R.L and Torrance, K.E., "A Reflectance Model for Computer Graphics", *ACM Transactions on Graphics*, Vol.1, 7-24, 1982.
9. Torrance K.E. and Sparrow, E.M., "Theory for Off-Specular Reflection for Roughened Surfaces", *J. Opt. Soc. Am.*, Vol.57, 1105-1114, 1967.
10. Beckmann, P. and Spezzichino, A., "The Scattering of Electromagnetic Waves from Rough Surfaces", MacMillan, New York, 1963.